Cite this article
Gaudio D, Seong J, Haigh S *et al.* (2023)
Boundary effects on dynamic centrifuge testing of onshore wind turbines on liquefiable soils.
International Journal of Physical Modelling in Geotechnics **23(1)**: 16–34,
https://doi.org/10.1680/jphmg.21.00085

Research Article
Paper 2100085
Received 18/10/2021;
Accepted 01/03/2022;
Published online 19/05/2022

International Journal of Physical Modelling in Geotechnics

ice Publishing

Boundary effects on dynamic centrifuge testing of onshore wind turbines on liquefiable soils

Domenico Gaudio MEng, PhD
Research Associate, Dipartimento di Ingegneria Strutturale e Geotecnica, Sapienza Università di Roma, Rome, Italy; formerly Department of Engineering, University of Cambridge, Cambridge, UK (Orcid:0000-0001-8957-5764) (corresponding author: domenico.gaudio@uniroma1.it)

Juntae Seong BEng
PhD student, Department of Engineering, University of Cambridge, Cambridge, UK

Stuart Haigh MEng, MA, PhD
Reader, Department of Engineering, University of Cambridge, Cambridge, UK (Orcid:0000-0003-3782-0099)

Giulia M. B. Viggiani MEng, PhD
Professor, Department of Engineering, University of Cambridge, Cambridge, UK (Orcid:0000-0002-0993-0322)

Gopal S. P. Madabhushi MTech, PhD (Cantab)
Professor, Department of Engineering, University of Cambridge, Cambridge, UK (Orcid:0000-0003-4031-8761)

Rajesh Shrivatsava MTech
Chief Operating Officer, Adani Green Energy Limited, Ahmedabad, India

Ravikant Veluvolu MTech
Vice President (Technology), Adani Green Energy Limited, Ahmedabad, India

Prashanta Padhy MTech
Deputy General Manager, Adani Green Energy Limited, Ahmedabad, India

Centrifuge modelling is an effective tool to assess the response of reduced-scale structures subjected to earthquakes under increased gravity. Space limitations, however, force the model to be contained within relatively small boxes, whose boundaries may affect the seismic performance of the structure under consideration. In this paper, the influence of the proximity of the boundaries of an equivalent shear beam (ESB) container during dynamic centrifuge tests of an onshore wind turbine resting on liquefiable soils is evaluated. To this end, numerical modelling of the ESB box was implemented in the finite-element framework OpenSees, to replicate the results observed in the experiment. The hydraulic and mechanical soil parameters were calibrated against far-field centrifuge results only. From this calibration, the seismic performance of the raft foundation turned out to be in good agreement with the experimental results for a seismic input capable of triggering liquefaction. A larger numerical model, where boundaries do not play any role, was then built, to compare its outcomes with those of the small model, thus allowing the effect of ESB boundaries to be assessed.

Keywords: centrifuge modelling/earthquakes/numerical modelling

Notation

$a_{x\ \max}^{\text{inp}}$	peak acceleration of the seismic input
$a_{x\ \max}^{\text{top}}$	peak acceleration at the top of the wind turbine
D	diameter of the raft foundation
D_{R}	relative density
$e_{\max}$	maximum void ratio
$e_{\min}$	minimum void ratio
f_{s}	fixed-base natural frequency of the wind turbine (= 0.30 Hz)
G_0	small-strain shear modulus of soil
G_{s}	specific gravity
$\boldsymbol{g}$	gravitational acceleration (= 9.81 m/s^2)
H_1	thickness of the clay layer (= 3.2 m)
H_2	thickness of the loose sand layer (= 15 m)
H_3	thickness of the dense sand layer (= 12 m)
h_{s}	height of the wind turbine (= 48 m)
J_{HEAD}	rotational inertia at the tip of the wind turbine
k	isotropic hydraulic conductivity of soil
m_{HEAD}	mass at the tip of the wind turbine
m_{tot}	total mass of the wind turbine
N	scaling factor adopted in the centrifuge test (= 80)
PSa	pseudo-acceleration
p	pore-water pressure
q	bearing pressure exerted by the structure on the loose sand layer (= 58.8 kPa)
s	thickness of the raft foundation
$V_{\text{S},0}$	small-strain shear wave velocity of soil
w_{ff}	far-field settlement
Δp	excess pore-water pressure
Δt	time increment
Δy	vertical distance between two adjacent nodes in the finite-element (FE) model
θ	rigid rotation of the raft foundation
$\lambda_{\min}$	minimum wavelength travelling into the FE model
ν	Poisson's ratio
ξ	damping ratio

ρ mass density
ϕ'_{cv} constant-volume friction angle

1. Introduction

Dynamic centrifuge modelling is a powerful tool for evaluating the seismic performance of structures subjected to strong seismic events. This is particularly true when assessing the liquefaction hazard of structures resting on loose, saturated sandy soils, as pointed out by several authors (Adamidis and Madabhushi, 2022; Dashti *et al.*, 2010; Esfeh and Kaynia, 2020; Karimi, 2016; Manzari *et al.*, 2018). Moreover, centrifuge testing is often adopted to calibrate numerical finite-element (FE) or finite-difference (FD) models that are subsequently used to perform extensive parametric studies (Chen *et al.*, 2021; Ramirez, 2019; Ramirez *et al.*, 2018).

Although very useful and widely adopted, the reliability of dynamic centrifuge testing still needs to be carefully evaluated and understood. Indeed, a major concern about centrifuge tests is the presence of the boundaries of the container the reduced-scale model is placed into, as they could play a role and affect the results obtained in the laboratory. In this context, Teymur and Madabhushi (2003) performed an experimental study in which the boundary effects generated with a previous version of the equivalent shear beam (ESB) container used at Cambridge University (Schofield and Zeng, 1992) were investigated. Their results indicate that these effects mainly induce amplification of motion caused by P-wave generation at the lateral walls, due to the stiffness contrast between the boundaries and the soil sample. In their study, boundary effects turned out to be minimal for dry and medium-dense sands (relative density $D_R = 50\%$) – that is, when the sandy sample is characterised by a stiffness similar to that the ESB container was designed for. However, in the presence of loose, saturated sand layers subjected to strong seismic shaking liquefaction may occur, thus increasing the stiffness contrast between the liquefied soil and the end walls. In this case, boundary effects may play a major role. The authors concluded that, in the presence of loose and saturated sandy soils, an estimation of the influence of the boundaries is necessary.

In this paper, the boundary effects of the most recent ESB container adopted at the University of Cambridge (Brennan and Madabhushi, 2002) are assessed. The results of a centrifuge test where an onshore wind turbine (OWT) on a raft foundation resting on liquefiable soils was subjected to one-directional ground motions were first taken as a reference. Numerical modelling of the ESB box containing the OWT and soil deposit was then performed using a three-dimensional (3D) FE numerical model implemented in the open-source OpenSees framework v 3.3.0 (McKenna *et al.*, 2000; Tarque Ruiz, 2020), so as to reproduce accurately the results obtained in the centrifuge. The two-phase nature of saturated soils was accounted for through the *u–p* formulation, based on the assumption of negligible soil–fluid relative acceleration (Zienkiewicz *et al.*, 1980). Cyclic sand behaviour was described through the advanced constitutive model Sanisand04 (Dafalias and Manzari, 2004), for which a calibration of Sanisand04 parameters for Hostun sand is not available in the literature, although being adopted for research purposes (Tsinidis *et al.*, 2015). The capability of Sanisand04 model to predict accurately sand behaviour in fully coupled problem has been clearly shown in the literature (Chen *et al.*, 2021) by a comparison with the PM4Sand model (Boulanger and Ziotopoulou, 2013), which provided quite similar results for high-intensity seismic shakings; further improvements may be anticipated thanks to new updates (Liu *et al.*, 2021; Yang *et al.*, 2022) The mechanical and hydraulic parameters of the soils were calibrated against the far-field centrifuge results only and they were then successfully used to reproduce the observed seismic performance of the structure. A larger numerical model was then built, in which the boundaries are far enough not to affect the response of the system, to compare its outcomes with those coming from the smaller numerical model. This permitted to assess the effects of ESB boundaries in a quantitative manner.

The findings presented in this study may be useful for engineers to interpret the results coming from centrifuge tests where liquefaction is triggered more confidently and with an increased awareness. Calibration of Sanisand04 parameters for Hostun sand against centrifuge tests is a further novel aspect of the paper.

2. Problem layout

Figure 1 shows the layout of the problem. An onshore wind turbine of height $h_s = 48$ m rests on a circular raft foundation with diameter $D = 15.4$ m and thickness $s = 1.6$ m. The tower is characterised by a total mass $m_{tot} = 435.8$ Mg (tons) and a fixed-base natural frequency $f_s \approx 0.3$ Hz, while the raft foundation rests on a fully saturated loose sand layer ($D_R = 43\%$) of thickness $H_2 = 15$ m, underlain by a dense sand layer ($D_R = 90\%$) of thickness $H_3 = 12$ m. The average contact pressure exerted by the structure on the sand layer is $q = 58.8$ kPa. The surface layer consists of a partially excavated clay ($H_1 = 3.2$ m), replaced with gravel in the vicinity of the foundation. The above-mentioned properties were selected to represent a typical configuration for an OWT on liquefiable soils.

The system is subjected at the base ($y = -30.2$ m) in the horizontal x-direction to a seismic motion intense enough to trigger liquefaction of the loose sand layer.

3. Dynamic centrifuge testing

A scaled model of the OWT was produced to simulate the prototype structure behaviour on the Turner beam centrifuge of

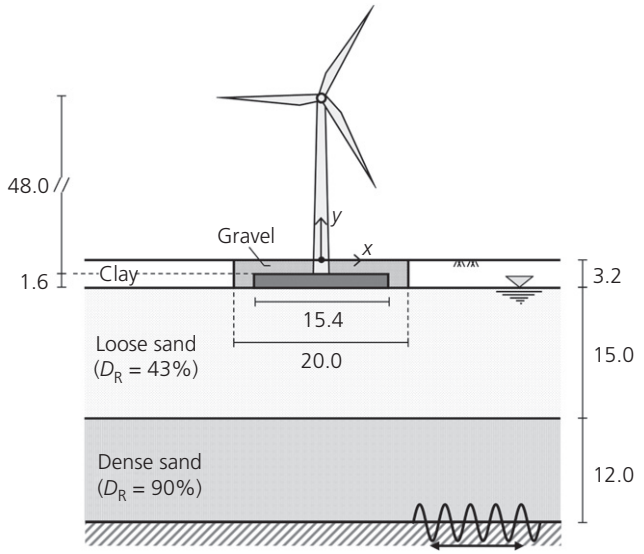

Figure 1. Schematic layout of the problem (dimensions in metres)

the Schofield Centre at the University of Cambridge, UK. The centrifuge model was prepared and spun at a nominal centrifugal acceleration of 80***g***.

The model container used was the most recent ESB box. In the reduced-scale model, the raft foundation is simulated by a circular aluminium plate, while the OWT is modelled using a steel hollow tube with a brass lumped mass at the top. At model scale, the raft foundation has a diameter of 192 mm (15.36 m at prototype scale) and a thickness of 20 mm (1.6 m), whereas the steel hollow tube has an outer diameter $D_{out} = 17.5$ mm (1.4 m) and a wall thickness $s_w = 2.5$ mm (0.2 m), thus being characterised by a bending stiffness $EI = 0.72$ kN m^2 (29.29 GN m^2). The head mass is $m_{HEAD} =$ 300 g (153.6 Mg). To produce the composite layer of sand, clay and gravel, the soil model was created in three steps. First, the sand layers were deposited in the box using a sand pourer. Second, the clay layer was made using pre-cut clay blocks. Third, gravel was placed in the gap where the raft foundation was located.

Hostun HN31 sand was adopted for the sand layers, whose physical properties are specific gravity $G_s = 2.65$, maximum and minimum void ratio, $e_{max} = 1.011$ and $e_{min} = 0.555$, respectively, and constant-volume friction angle $\phi'_{cv} = 33°$. The target relative densities were obtained by air pluviation using the sand pourer available at the Schofield Centre (Madabhushi *et al*., 2006). After pouring, the sand layers were fully saturated using an aqueous solution of hydroxypropyl methylcellulose (Adamidis and Madabhushi, 2015), with a viscosity of 80 MPa s.

The model layout is shown in Figure 2(a) together with the location of sensors. Arrays of piezo-electric accelerometers (red arrows in Figure 2) and pore-pressure transducers (PPTs, blue ellipses in Figure 2) were installed in the centre of the box beneath the structure and along a vertical between the structure and the side wall, meant to represent far-field conditions. Sensors located in the same position were installed at a distance of at least 25 mm (2 m) from one another to reduce the interference from the sensor body. A linear variable differential transformer (LVDT) was positioned at the clay surface to measure the far-field settlement w_{ff} and an air hammer was installed at the bottom of the box to perform air hammer tests (AHTs; Ghosh and Madabhushi, 2002) in flight, to obtain the shear wave velocity $V_{S,0}$ of the soil deposit and its small-strain shear modulus G_0, through the well-known relation:

$$1. \quad G_0(z) = \rho \times \left[V_{S,0}(z)\right]^2$$

where ρ is the mass density of soil. The experimental values of the small-strain shear modulus obtained along the far-field alignment are plotted in Figure 2(b) (black crosses).

Horizontal (H1, H2, H3 and H4 in Figure 2(a)) and vertical (V1, V2, V3 and V4) accelerations were also measured on both the model structure's head and foundation using micro-electrical-mechanical systems (MEMS) accelerometers. Two LVDTs were positioned on the foundation, each at a distance of 70 mm (5.6 m) on either side of the central axis, to measure both the settlements and the rigid rotation of the foundation during the test.

4. 3D FE modelling

In this section, the results of 3D non-linear dynamic FE analyses performed in the time domain are shown and discussed. First, the characteristics of the FE model reproducing the experimental set-up with the ESB container size (small model in the following) are reported. This model was adopted to calibrate both the hydraulic and mechanical parameters of the sand layers, so as to be representative of the centrifuge test. Then, a much larger numerical domain (large model), where wall ends do not affect the seismic performance of the OWT, was developed, to quantify the boundary effects of the ESB container. Unless otherwise stated, all dimensions in the following are given at prototype scale.

4.1 Small model reproducing the ESB container

The small 3D model is represented in Figure 3(a). Following the centrifuge test, the seismic input was applied in the x-direction only, making it possible to consider half of the domain thanks to problem symmetry. Model dimensions are the same as the ESB container at prototype scale ($N = 80$), that is

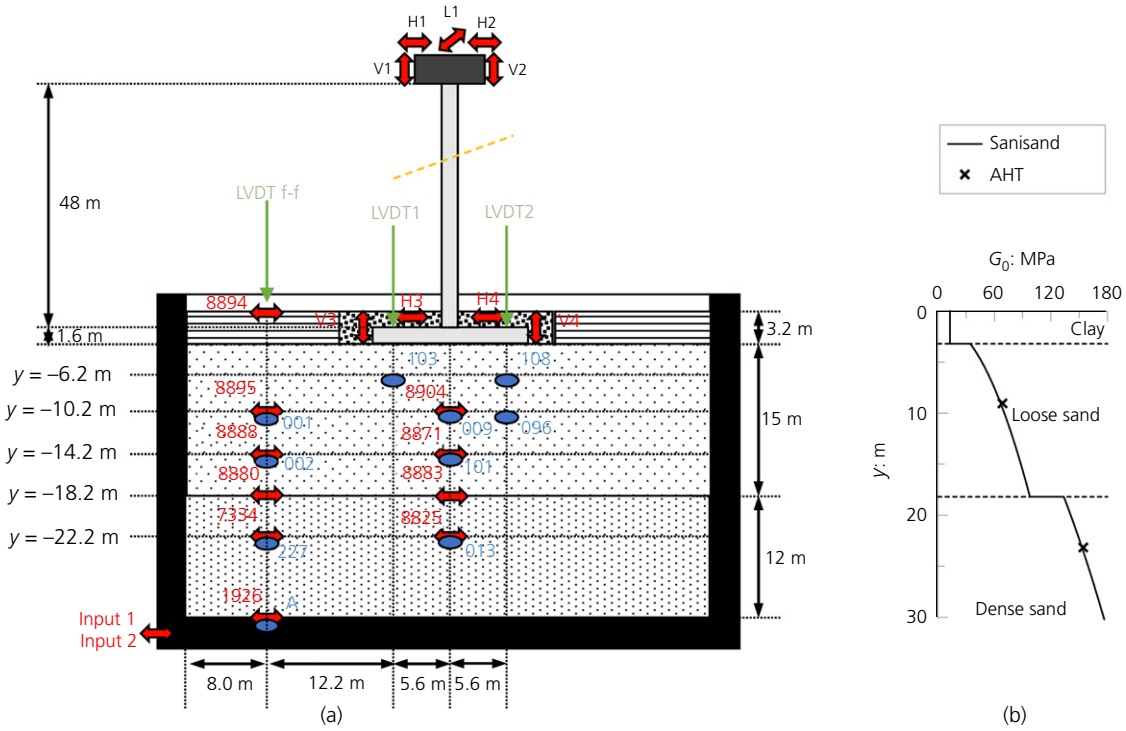

Figure 2. Model layout for the centrifuge test: (a) layout of instrumentation and (b) far-field small-strain shear modulus profile from AHT and calibrated Sanisand model (prototype units)

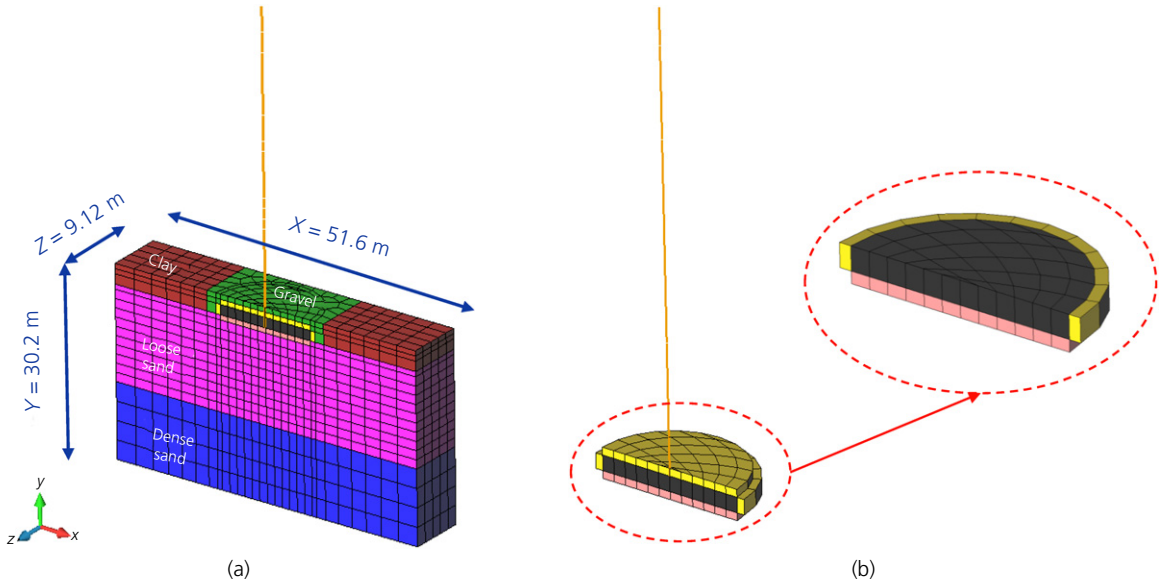

Figure 3. Small 3D FE domain: (a) overall mesh and (b) detail of the tower and the raft

$X = 51.6$ m ($\approx 3.4 \times D$), $Z = 9.12$ m ($\approx 1.2 \times D/2$) and $Y = 30.2$ m ($\approx 2 \times D$). The FE mesh is made of 2401 elements and 3121 nodes, with a progressively finer mesh approaching the raft foundation, and particularly at the soil–foundation interface, where thin continuum layers were placed (Figure 3(b)) to assign materials of 'degraded' mechanical properties (Griffiths, 1985). Thickness of the interface layers was imposed equal to $5\%D \approx 0.8$ m (Pisanò, 2019).

BrickUP elements were adopted to discretise the whole domain (Yang *et al.*, 2008). These are hexahedral linear isoparametric elements that were developed on purpose for saturated soils, for which the *u–p* formulation (Zienkiewicz and Shiomi, 1984) is adequate when soil–fluid relative acceleration can be neglected. The size of the finite elements adopted for soils were selected to fulfil the requirement provided by Kuhlemeyer and Lysmer (1973), therefore avoiding numerical distortion of waves propagating into the model. To this end, it was checked that the vertical distance between two adjacent nodes, Δy, satisfies at every depth, the condition:

$$2. \quad \Delta y \leq \frac{\lambda_{\min}}{6} = \frac{V_S}{6 \times f_{\max}}$$

where $\lambda_{\min}$ is the minimum wavelength expected within the FE model, V_S is the soil shear wave velocity and $f_{\max} = 4$ Hz is the maximum frequency of the seismic input. At every depth, the shear wave velocity was evaluated from the profile obtained from the Sanisand04 constitutive model, calibrated against the AHT results (Figure 2(b)).

In the initial static (gravity) calculation phase, standard boundary conditions were applied to the model – that is, $u_x = 0$ along the lateral *y–z* boundaries, $u_z = 0$ along the *x–y* boundaries and fixed nodes at the base of the mesh ($u_x = u_y = u_z = 0$). When switching to the dynamic calculation phase, the restraints on the horizontal displacements at the base of the mesh were removed and the seismic input was applied in terms of the horizontal acceleration time history – that is, assuming that the bedrock is infinitely rigid (fully reflecting boundary). The seismic input, shown in Figure 4(c), is the same as that applied in the centrifuge test, representing a high-intensity sinusoidal acceleration time history characterised, at prototype scale, by a peak acceleration $a_x^{\text{inp}}{}_{\max} \approx 0.2\boldsymbol{g}$, a frequency $f = 1$ Hz and a total duration of 10 s (i.e. ten cycles). During the dynamic calculation phase, periodic constraints (Zienkiewicz *et al.*, 1988) were applied to the nodes on the lateral *y–z* boundaries of the mesh – that is, the nodes were free to move in the horizontal *x*-direction, while tied to one another in order to enforce the same displacements of the two boundaries ($\Delta u_x = 0$). This corresponds to imposing free-field pure-shear conditions at the lateral boundaries, such as those applied by the end walls of the ESB container.

Hydraulic boundary conditions were set with the water table located at the top of the loose sand: pore-water pressures were allowed to fluctuate freely for all nodes within the sand layers ($y \leq -3.2$ m), while both steady and excess pore-water pressures were inhibited in the clay and gravel layers ($p = \Delta p = 0$) – that is, any capillary suctions were neglected.

Soil constitutive models and relevant parameters were calibrated against the far-field centrifuge results, as discussed in the following section (Section 4.1.1), while the mechanical behaviour of both the aluminium raft and the steel tower was prescribed using an isotropic linear-elastic model, whose parameters are listed in Table 1, where ρ is the mass density, E is the Young's modulus and ν is the Poisson's ratio. The tower was modelled through 60 0.8 m-long Timoshenko beam elements. Because of symmetry, the lumped nodal mass at the tip of the tower is half the mass in the physical model ($m_{\text{HEAD}} = 153.6/2 = 76.8$ Mg). Moreover, the node at the tip was assigned the rotational inertia of the brass mass ($J_{\text{HEAD}} = 480.06/2 = 240.03$ Mg m^2), in order to reproduce the centrifuge test as closely as possible.

The 3D non-linear dynamic analyses were performed selecting as a maximum time increment $\Delta t = 0.0133$ s and varying it during the computation to obtain convergence and fulfil the criterion proposed by Haigh *et al.* (2005). This required that the time increment be subdivided up to 32 times (i.e. down to $\Delta t \approx 0.0004$ s) when soil approached liquefaction. The dynamic analyses lasted for up to 15 s. Newmark's time-stepping method (Newmark, 1959) was used to integrate the equations of motion with values $\beta = 0.60$ and $\gamma = 0.3025$, while the Krylov–Newton solution algorithm (Scott and Fenves, 2010) was selected to handle non-linear soil behaviour.

4.1.1 Soil constitutive models and calibration of hydro-mechanical parameters

The mechanical behaviour of the soils was modelled using three different advanced constitutive models, namely the pressure-independent multi-yield (PIMY) model for the clay layer, the pressure-dependent multi-yield (PDMY) model (Yang *et al.*, 2003) for the gravel layer, and Sanisand04 (Dafalias and Manzari, 2004) for the loose and dense sand layers. For the clay and gravel layer, the values of model parameters provided by Yang *et al.* (2008) were adopted, assuming a soft clay and a medium-dense sand ($D_R = 65$–85%) behaviour, respectively (Tables 2 and 3).

For the loose and dense sand layers, Sanisand04 model parameters were first obtained from Salvatore *et al.* (2017), who calibrated the constitutive parameters against triaxial tests on samples of Hostun sand, and then further calibrated to match the excess pore-water pressure build-up and dissipation measured during the centrifuge test along the far-field array

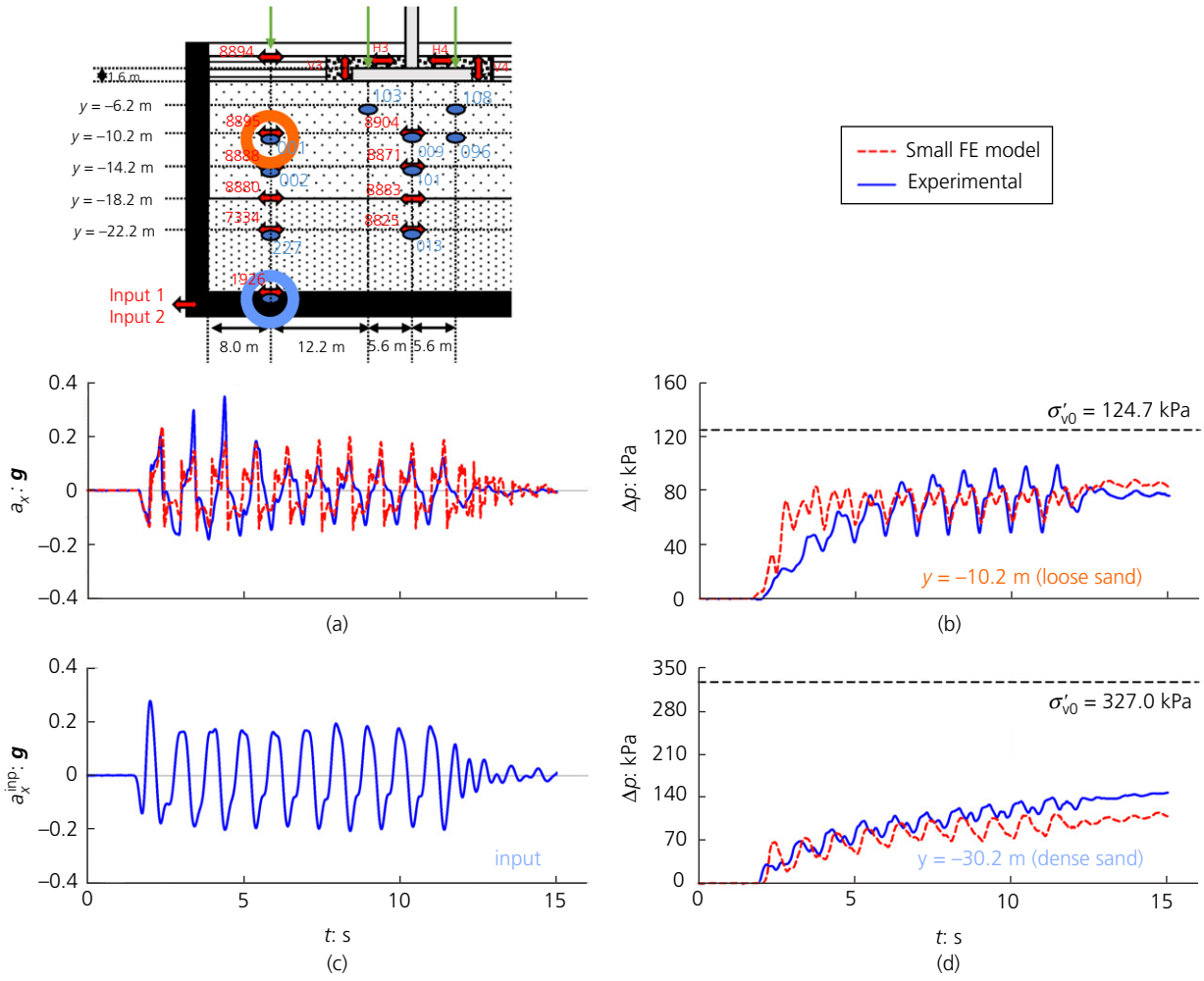

Figure 4. Time histories of total horizontal acceleration and excess pore-water pressure in the far field for: (a–b) loose sand layer (depth $y = -10.2$ m) and (c–d) dense sand layer ($y = -30.2$ m)

Table 1. Values assumed for the isotropic linear elastic media adopted for the raft and the tower

Body	ρ: Mg/m^3	E: GPa	ν: dimensionless
Raft	2.70	70.0	0.15
Tower	7.80	210.0	0.30

(Table 4). The value of G_0 turned out to be in agreement with that provided by Azeiteiro *et al.* (2017). The hydraulic conductivity, k, is a property of the BrickUP finite elements and not of the Sanisand04 constitutive model. This was reduced by about six times with respect to Kassas *et al.* (2021) to match the excess pore-water pressure dissipation after the end of the earthquake; adjustments to permeability to account for microstructural changes taking place during liquefaction have been previously investigated by Haigh *et al.* (2012). In particular, k was taken to be 1.48×10^{-4} and 6.74×10^{-5} m/s for the loose and dense sand, respectively. For both gravel and loose sand interfaces, stiffness moduli were reduced by a factor of 2/3, while the shear strength was reduced by a factor of 3/4 (Kementzetzidis *et al.*, 2019).

A small amount of damping ($\xi_{soil} = 1\%$) was added through the Rayleigh formulation to attenuate the effect of spurious high frequencies that may arise in the domain. The raft foundation and the turbine were assigned damping ratios $\xi_{raft} = 1\%$ and $\xi_{turbine} = 3\%$, respectively, the latter being calibrated against experimental free vibrations.

Following this calibration process for soil parameters, the results of the numerical analyses obtained from the small

Table 2. Values of PIMY parameters assumed for the clay layer

ρ: Mg/m^3	G^{ref}: MPa	K^{ref}: MPa	c: kPa	γ_{max}: dimensionless	ϕ: °	d: dimensionless
1.3	13.0	65.0	18.0	0.1	0.0	0.0

numerical model were in good agreement with the results of the centrifuge test carried out in the ESB container. Figure 4 shows the time histories of the total horizontal acceleration (a) and excess pore-water pressure (b, d) obtained into the loose (depth $y = -10.2$ m) and dense ($y = -30.2$ m) sand layers along the experimental and numerical far-field array. The main aim of the calibration of Sanisand04 mechanical parameters and hydraulic soil parameters was to reproduce the time history of excess pore-water pressure, $\Delta p\ (t)$ developed into the loose sand layer (Figure 4(b)). Although the computed seismic-induced pore-pressure build-up is slightly faster than in the centrifuge test, both the peak values of excess pore-water pressure (≈80 kPa against 100 kPa, with a difference of about 20%) and the frequency content are well reproduced by the numerical analyses. The beginning of post-seismic re-consolidation, corresponding to the final part of the plots in Figure 4(b), in which the numerical and experimental time histories are almost parallel, is also adequately reproduced. Similar conclusions may be drawn for the excess pore-water pressures in the dense sand layer (Figure 4(d)), even if the final value of the computed excess pore-water pressure in this layer, 105 kPa, is somewhat smaller than the observed value (140 kPa). The acceleration time histories recorded into the loose sand layer were satisfactorily captured as well (Figure 4(a)), except for some spikes obtained in the centrifuge between 2.5 and 5 s, which may be attributed to densification occurring into the loose sand and which cannot be reproduced by the numerical model. The proposed calibration was verified against the results obtained for other seismic inputs, corresponding to acceleration time histories recorded during real earthquakes, which were applied in the centrifuge tests. However, for the sake of brevity, the comparisons are not shown in this paper.

The above-mentioned calibration of soil parameters supported the 'blind' prediction of the wind turbine seismic performance (Figure 5). The observed absolute settlement, w, of the raft foundation was almost perfectly matched by the FE analysis on the left side (Figure 5(a)), in terms of both its permanent value (0.34 m in the FE analysis and 0.33 m in the centrifuge) and rate of accumulation, whereas slight differences are observed in its frequency content. Unfortunately, LVDT_2 malfunctioned during the test, so that the experimental values of the settlement of the foundation on the right side were not available. The data reported in Figure 5(b) are an estimate of the settlement of the foundation on the right side, obtained from the measurement of LVDT_1, assuming that the instantaneous point of rotation of the foundation was the same as the numerical one. The seismic performance of the raft is given in Figure 5(c) in terms of the relative average settlement with respect to the far-field settlement, the latter measured at ground surface. Here, the numerical time history shows some deviation from the experimental one, but the comparison is still satisfactory (0.42 m from the FE model against 0.45 m obtained experimentally, a difference of 7%). Finally, the counter-clockwise rotation of the raft foundation (Figure 5(d)) was computed as

$$\theta(t) = \frac{[w_1(t) - w_2(t)]}{d_{12}} \quad (3)$$

where w_1 and w_2 are the settlements at the left and right side of the foundation and $d_{12} = 11.2$ m is the distance between the two LVDTs. Overall, the experimental time history of foundation rotation is captured satisfactorily by the numerical analysis. A peak value of rotation of −0.2° is computed both from the experimental results and in the numerical analysis, even if the frequency contents of the numerical and experimental time traces are somewhat different.

Figure 6 shows the experimental and numerical values of the excess pore-water pressures developed beneath both sides of the raft foundation. The numerical predictions obtained for the left side of the foundation (Figure 6(a)) are in very good agreement with the observations, with almost the same final value and a closely matched time history. In contrast, even if the final value of the excess pore-water pressure computed beneath the right edge of the foundation is similar to the experimental value, in this case the numerical FE small model predicted a faster development of excess pore-water pressures (Figure 6(b)). This may explain why, although the computed permanent settlement and rotation were very similar to the observed ones, the rate of accumulation of raft rotation computed using the small FE model was faster than the observed one.

Finally, Figure 7 shows the numerical and experimental horizontal acceleration time histories (Figure 7(a)) and elastic pseudo-acceleration spectra (damping ratio $\xi = 5\%$, Figure 7(b)) at the top of the wind turbine. Again, the comparison is satisfactory in terms of both the peak acceleration (about 0.12$\boldsymbol{g}$) and the frequency content. As for the latter, the pseudo-acceleration spectra show two peaks at periods $T = 0.44$ s and $T = 1.00$ s, corresponding to the second eigen-period of the

Table 3. Values of PDMY parameters assumed for the gravel layer

ρ: Mg/m^3	G^{ref}: MPa	K^{ref}: MPa	ϕ: °	ϕ_{PT}: °	γ_{max}: dimensionless	d: dimensionless	c: dimensionless	d_1: dimensionless	M: dimensionless	d_2: dimensionless	l_1: kPa	l_2: dimensionless	l_3: dimensionless	n: dimensionless	e: dimensionless
2.0	100.0	300.0	37.0	27.0	0.1	0.5	0.05	0.6	3.0	3.0	5.0	0.003	1.0	20	0.55

Table 4. Calibrated values of Sanisand parameters adopted for the sand layers

Sand	e_{init}: dimensionless	ρ: Mg/m^3	G_0: dimensionless	ν: dimensionless	M: dimensionless	c: dimensionless	e_0: dimensionless	λ_c: dimensionless	ξ: dimensionless
Loose	0.813	1.947	293.0	0.05	1.30	0.712	1.13	0.13	0.45
Dense	0.600	2.071							
m: dimensionless	h_0: dimensionless	c_h: dimensionless	n^b: dimensionless	A_0: dimensionless	n^d: dimensionless	z_{max}: dimensionless			c_z: dimensionless
0.02	1.82	0.968	1.1	0.33	3.5	10.0			1000

system and to the main period of the seismic input, respectively; the fundamental period of the system, $T_s = 0.30$ s, is not excited by the applied seismic input. However, non-negligible differences are observed in the acceleration time histories of the tower during the free-oscillations at the end of the seismic input ($t = 12.5$–15 s) and in the pseudo-acceleration spectra at the above-mentioned periods. This may be attributed to the Rayleigh damping formulation adopted for the turbine, which underdamps the system in between the selected controlling frequencies while overdamping out of this frequency range: here the choice of the target frequencies was directed towards the correct simulation of the peak acceleration (i.e. PSa at $T = 0$), which is well reproduced in the numerical analyses indeed.

4.2 Dynamic analysis using the large numerical model

The boundary effects of the ESB container in the presence of loose, saturated sandy soils were assessed through the comparison of the results obtained with the small numerical model, deemed representative of the ESB container, with those obtained from the large 3D model shown in Figure 8. This domain simply constitutes an extension of the small model in the x and z direction: new dimensions are equal to $X = 150$ m ($\approx 10 \times D$) and $Z = 75$ m ($\approx 5 \times D$), which were selected to ensure that model boundaries were far enough from the structure not to affect its dynamic behaviour. The FE mesh now consists of 12 013 elements and 13 780 nodes, with the same hydraulic and mechanical boundary conditions as those already discussed in Section 4.1.

As shown in Figure 9, the results of the numerical analysis with the large model were extracted at the same locations of the instruments in the centrifuge test (Figure 2) with the addition of a free-field alignment ($x = -39.0$ m), which is likely not to be affected by either the structure or the boundaries of the large numerical model. The original far-field alignment ($x \approx -17.0$ m) is not likely to be affected by the boundaries of the large model, but it might be affected by the structure. Therefore, a comparison of the results obtained along the free-field and far-field alignments in the large model can be used to quantify the influence of the structure on the far-field results. In contrast, a comparison between the results of the large and small models along the far-field arrays can shed some light on the influence of the boundaries on the far-field results in the small model (and therefore on the ESB box).

Figure 10 shows the time histories of the horizontal acceleration and excess pore-water pressure computed in the free field and far field using the large FE model. It is evident that the results almost overlap at all depths, with some acceptable discrepancies in the peak values of horizontal acceleration at ground surface (Figure 10(a)), of the order of 10%. The same results are shown

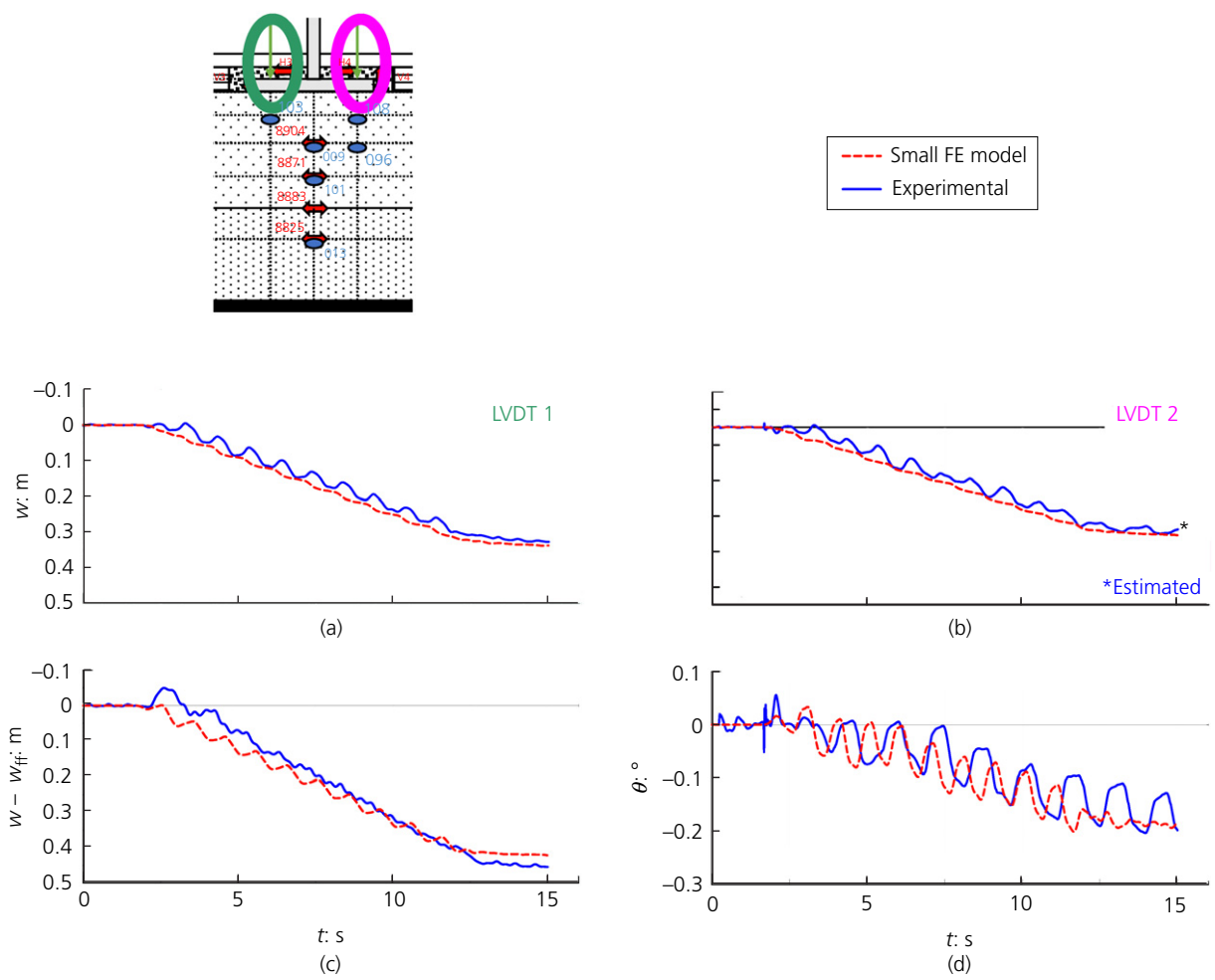

Figure 5. Experimental and numerical time histories of: (a–b) settlements measured at the foundation edges, (c) average settlement relative to the far field and (d) foundation rotation

in Figure 11 in terms of profiles of peak quantities. In particular, Figure 11(a) shows the profile of the ratio of the peak acceleration, $a_{x\ \max}$, to the peak acceleration of the input motion, $a_{x\ \max}^{\text{inp}}$, while Figure 11(b) shows the profile of the maximum computed excess pore-water pressure. The comparison between the free field and far field is very good even in terms of peak values of acceleration ratio and excess pore-water pressure, confirming that, despite its proximity to the structure (about 10 m or $\approx 0.6 \times D$, see Figure 2), the far-field alignment is representative of the free-field soil response.

5. Assessment of boundary effects on the OWT seismic performance

The results obtained using the large and small numerical models can be used to assess the significance of boundary effects in the ESB container.

Figure 12 shows the contours of the norm of the displacement relative to the base $|u|$ computed using the two models at the end of the dynamic calculation phase ($t = 15$ s). The results in Figure 12(b) are only those in the centre of the large model, corresponding to the dimensions of the small model. The displacements obtained using the small FE model (representative of the ESB container) are slightly larger than those obtained using the large FE model, particularly close to the boundaries and at left the edge of the foundation, which may cause slightly higher raft rotations. Figure 13 shows the contours of the excess pore-water pressure accumulated at the end of the dynamic calculation phase ($t = 15$ s), as computed using the small and the large model. As before, Figure 13(b) shows only the central portion of the large model. Larger values of excess pore-water pressures can be observed in the small model at the loose–dense sand interface, possibly caused by higher shear strains γ due to the ratio of impedances between the two sand

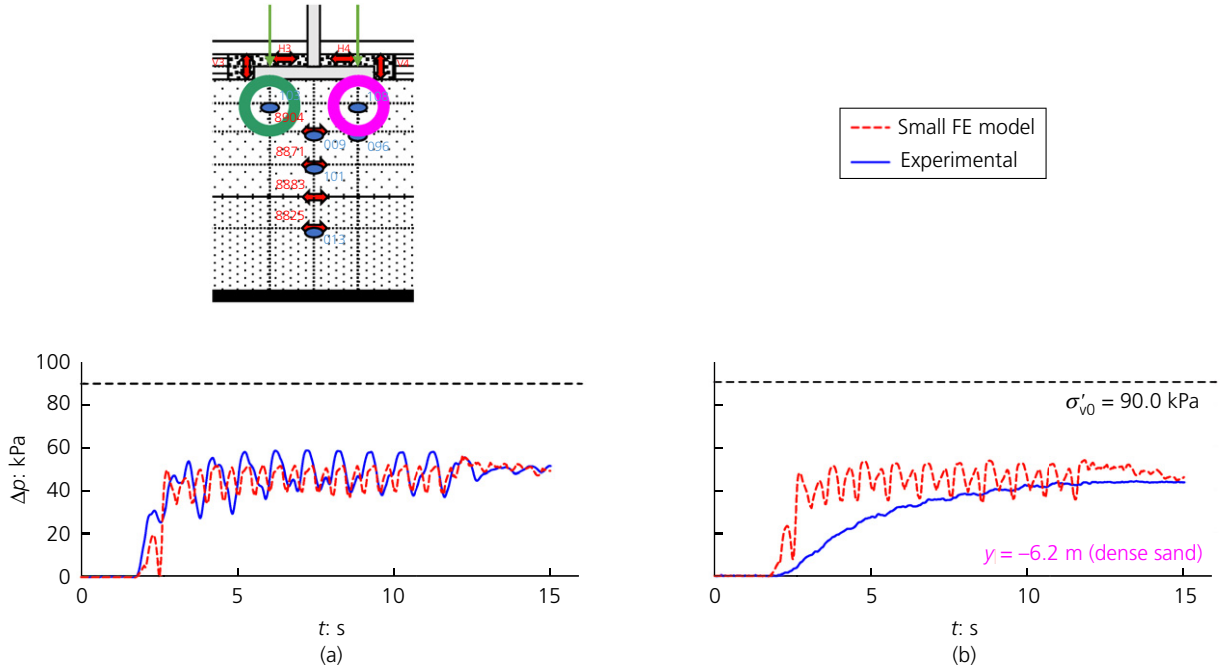

Figure 6. Comparison of excess pore-water pressure time histories obtained beneath (a) left and (b) right edge of the raft foundation

layers. Despite the small differences described above, however, overall the results obtained from the small and large models are quite similar throughout the numerical domain. This implies that, on average, boundary effects did not affect significantly the OWT response.

Similarly, a good agreement between the small and large FE model results is seen in Figure 14, where the time histories of horizontal acceleration (Figure 14(a)) and excess pore-water pressure (Figure 14(b)) computed into the loose sand layer along the far-field alignments are shown together with the results from the centrifuge test. The predictions obtained from the large model resemble strongly those from the small model, although some modest deviation is observed in terms of the values of Δp at the end of the dynamic calculation phase.

The main difference in the results from the small and large models resides in the predicted values of the absolute settlement experienced by the clay at the far-field ground surface, w_{ff} (Figure 15(a)). Heave of about 0.1 m is both observed in the centrifuge test and predicted by the FE analysis using the small model, whereas a settlement of about 0.03 m is computed using the large FE model. The surface heave in the far field is due to boundary effects affecting both the small FE model and the centrifuge physical model and causing excess pore-water pressures at the loose–dense sand interface.

The observed discrepancy in the far-field settlement implies a different evaluation of the OWT seismic performance, as shown in Figure 15(d) in terms of the relative average settlement $w–w_{ff}$. In fact, permanent relative settlements from the small and the large models are equal to 0.42 and 0.31 m, respectively, corresponding to a difference of about 27%. This difference is only due to the already-discussed differences in the computed values of the free-field settlement, as confirmed by the prediction of the absolute raft settlement shown in Figures 15(b) and 15(c), where the results obtained with the small and large FE models are practically the same. The final rigid rotation of the raft (Figure 15(d)) computed with the large model was also smaller than that predicted using the small model, with a value of 0.12° compared to 0.20°, or a difference of about 40%. Although boundary effects affected the evaluation of the seismic performance of the OWT, the absolute difference of the predicted rotation is only 0.08°, which can be deemed negligible if compared with the threshold permanent tilt of about 0.50–0.75° typically allowed for wind turbines (Kaynia, 2019).

The OWT seismic performance can be assessed in terms of the peak horizontal acceleration acting at the top of the tower, $a_{x\,\max}^{top}$, which can be retrieved from both the time history of horizontal acceleration and from the elastic pseudo-acceleration spectra plotted in Figure 16, and is equal to $0.11\boldsymbol{g}$ and $0.10\boldsymbol{g}$ with the small and large models, respectively

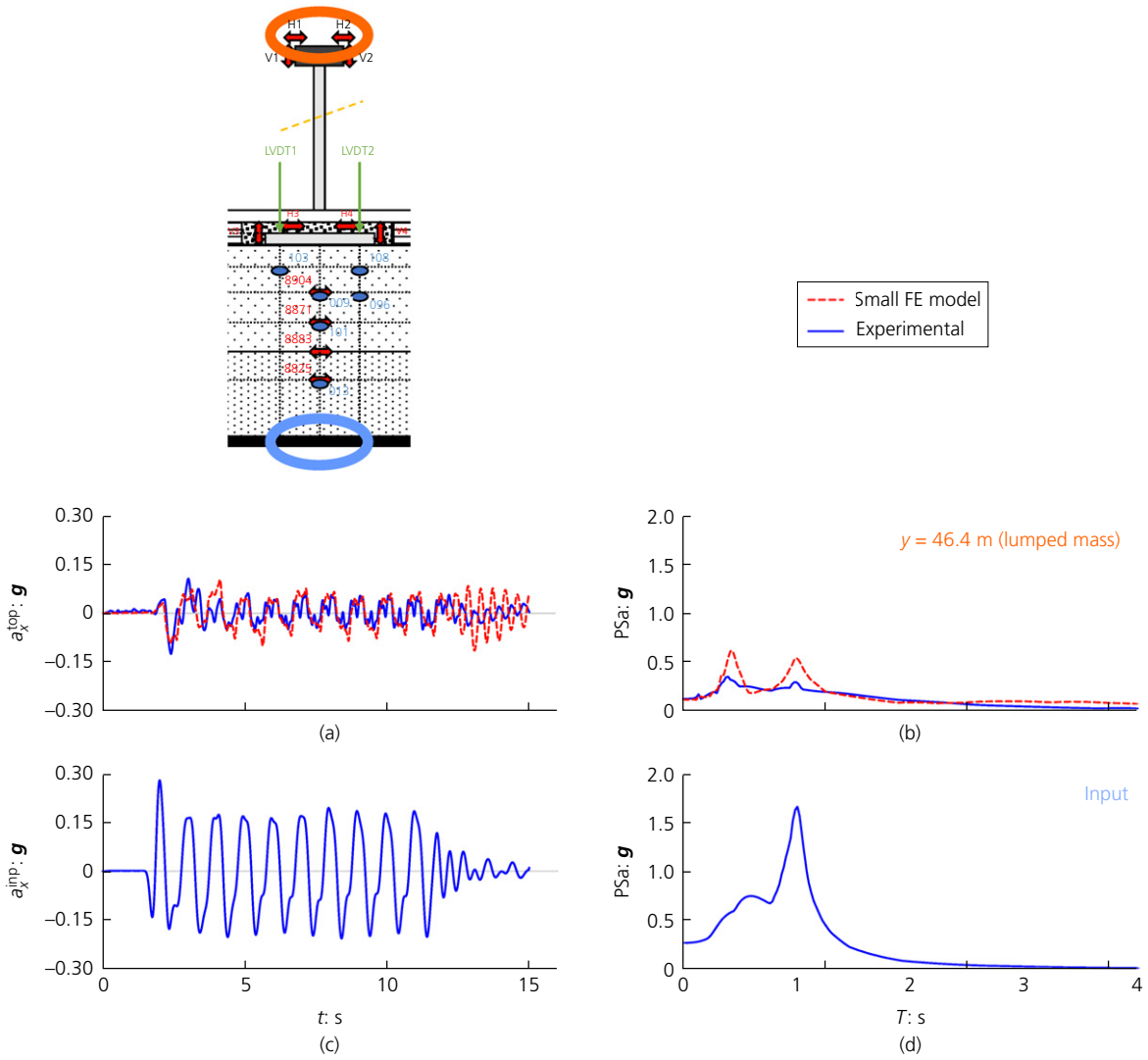

Figure 7. Total horizontal acceleration time histories and elastic acceleration spectra (a–b) obtained at lumped mass level and (c–d) of the input motion

(≈10% difference). The results show that the acceleration time history and long-period response of the wind turbine predicted using the small and large models are nearly identical, whereas the short-period (i.e. high-frequency) behaviour is slightly influenced by the presence of the boundaries. Indeed, the horizontal acceleration detected at the first peak of the spectrum ($T = 0.44$ s) is moderately amplified in the small model, with a value of $0.61\boldsymbol{g}$ compared to the value of $0.51\boldsymbol{g}$ computed using the large model. This confirms that boundary effects were responsible for an increase of high-frequency components of inertial forces transmitted to the wind turbine.

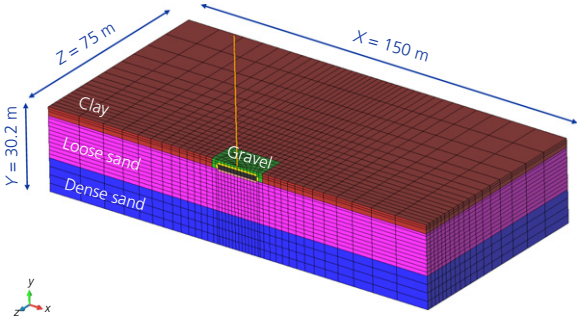

Figure 8. Large 3D FE domain

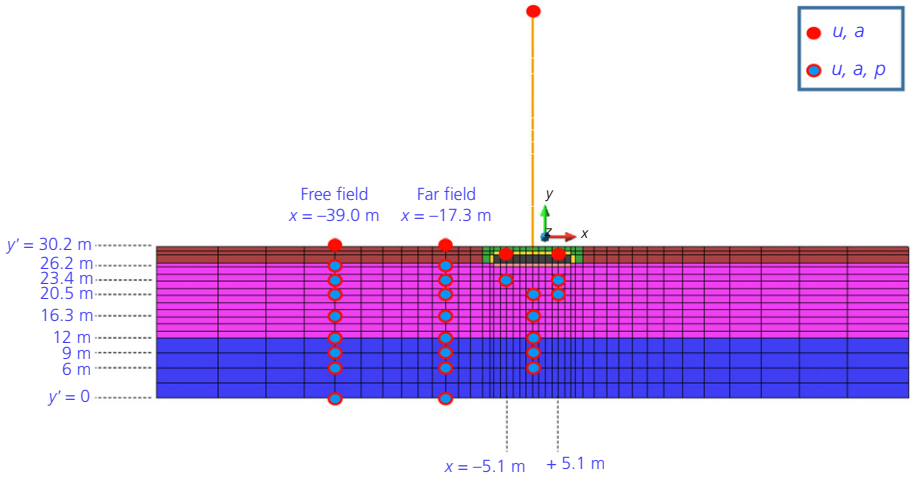

Figure 9. Output schematics adopted in the numerical analyses performed with the large numerical domain

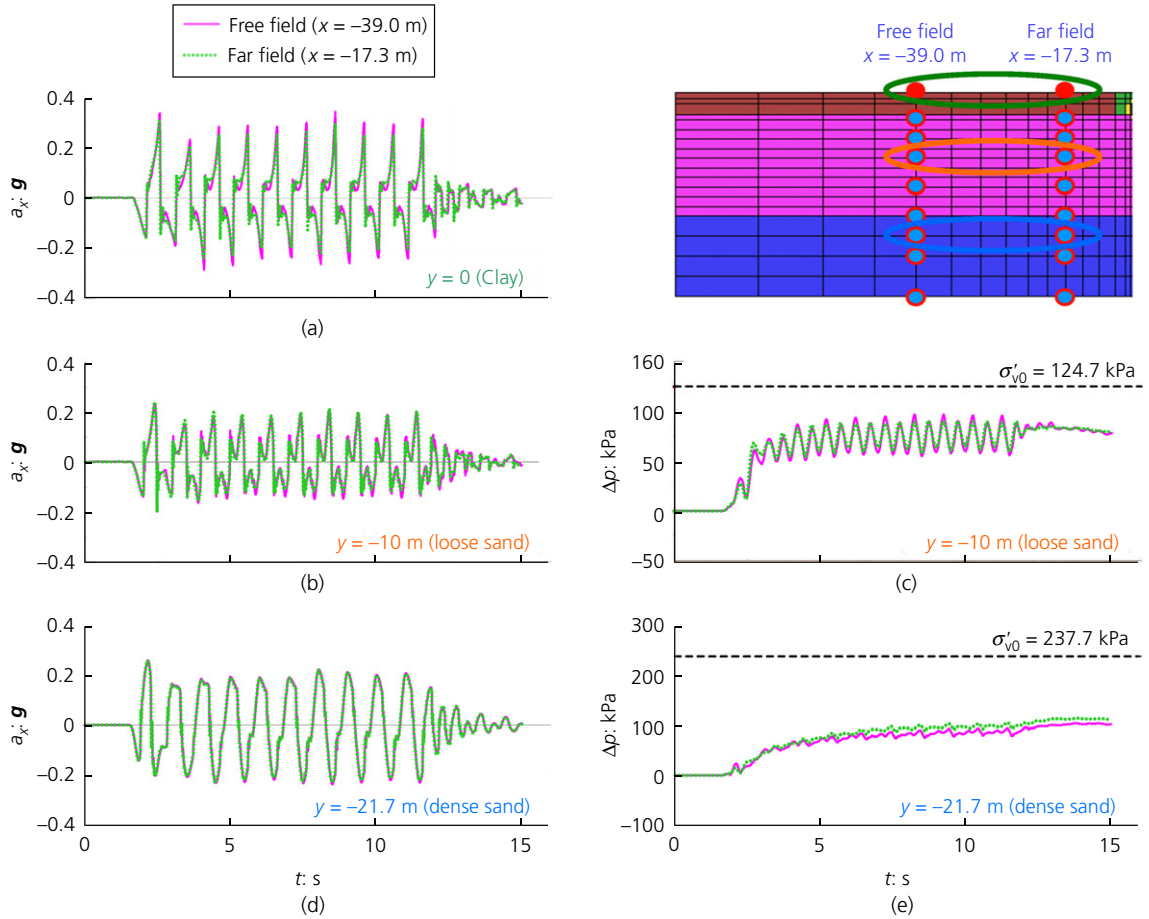

Figure 10. Time histories of (a, b, d) total horizontal accelerations and (c, e) excess pore-water pressures computed along the far-field and free-field alignments with the large FE model

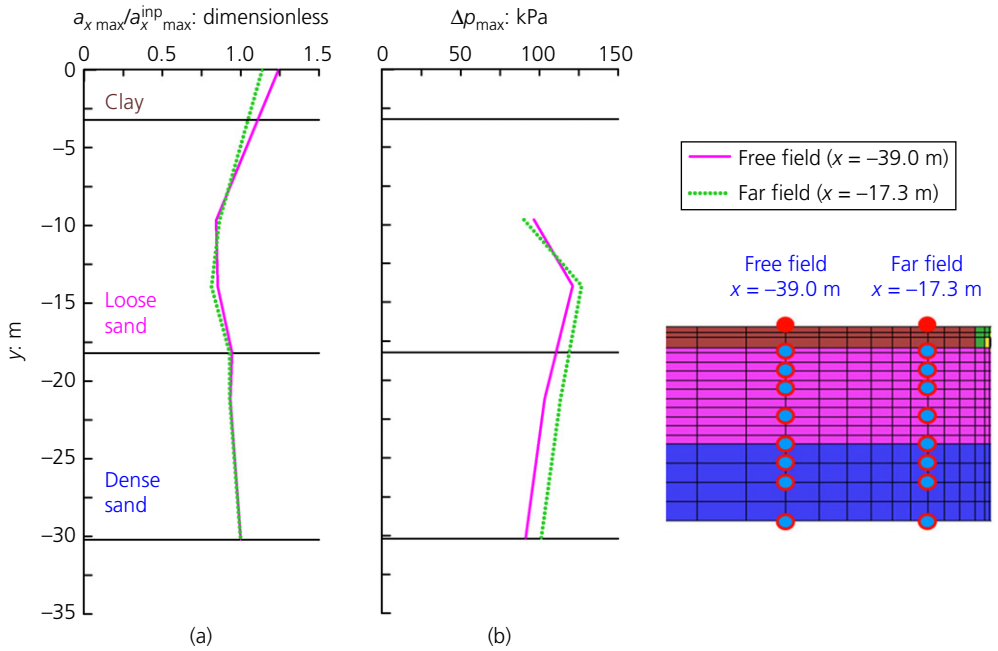

Figure 11. Profiles of (a) peak acceleration ratio and (b) excess pore-water pressure computed along the far-field and free-field alignments with the large FE model

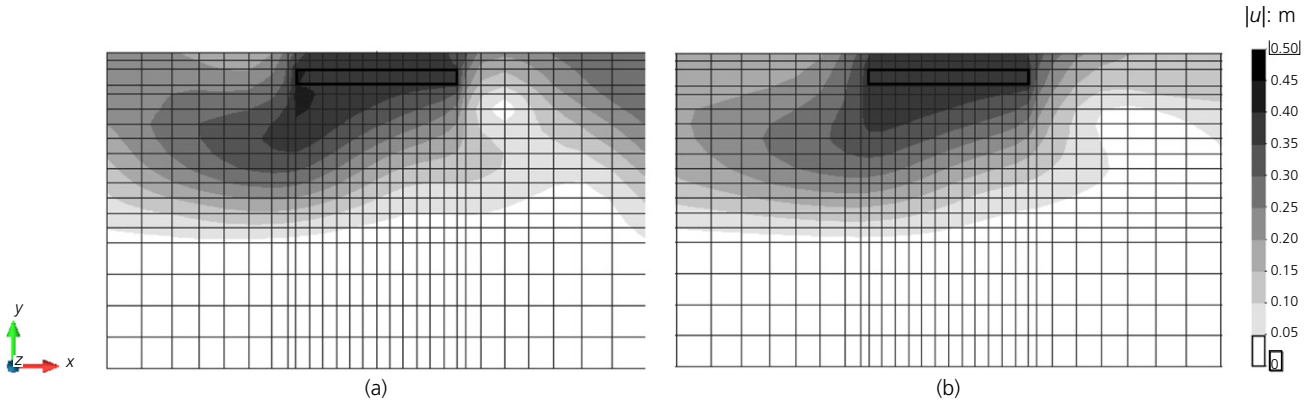

Figure 12. Contours of displacement relative to the base computed at the end of the dynamic calculation phase ($t = 15$ s) close to the raft foundation: (a) small and (b) large FE models

The values attained by the seismic performance indexes discussed above are summarised in Table 5, where the ratio large/small is also listed to give an insight of the influence of boundaries on the seismic performance. These values are plotted in Figure 18 as well, for (a) the raft foundation and (b) the wind turbine: in this figure it is pointed out that the best prediction is obtained for the wind turbine, while the performance of the foundation results to be affected by the presence of the boundaries: this is particularly true for the rigid rotation of the raft. However, values from the small model (and then from the ESB container adopted in the centrifuge) are always higher than those from the rigorous large model, thus providing an estimate of the seismic performance to be on the safer side.

Similar conclusions can be drawn from the results obtained applying two additional seismic inputs at the base of the small

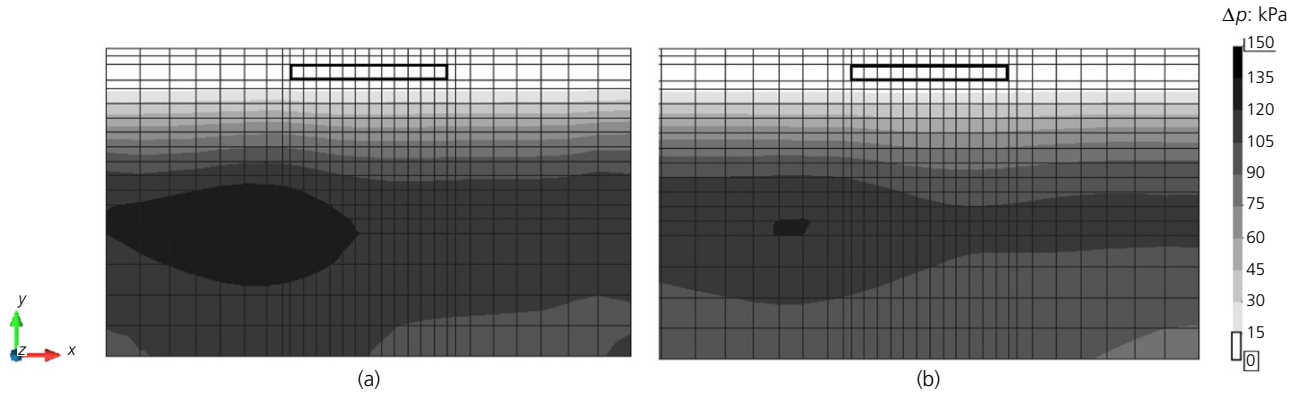

Figure 13. Contours of excess pore-water pressure computed at the end of the dynamic calculation phase ($t = 15$ s) close to the raft foundation: (a) small and (b) large FE models

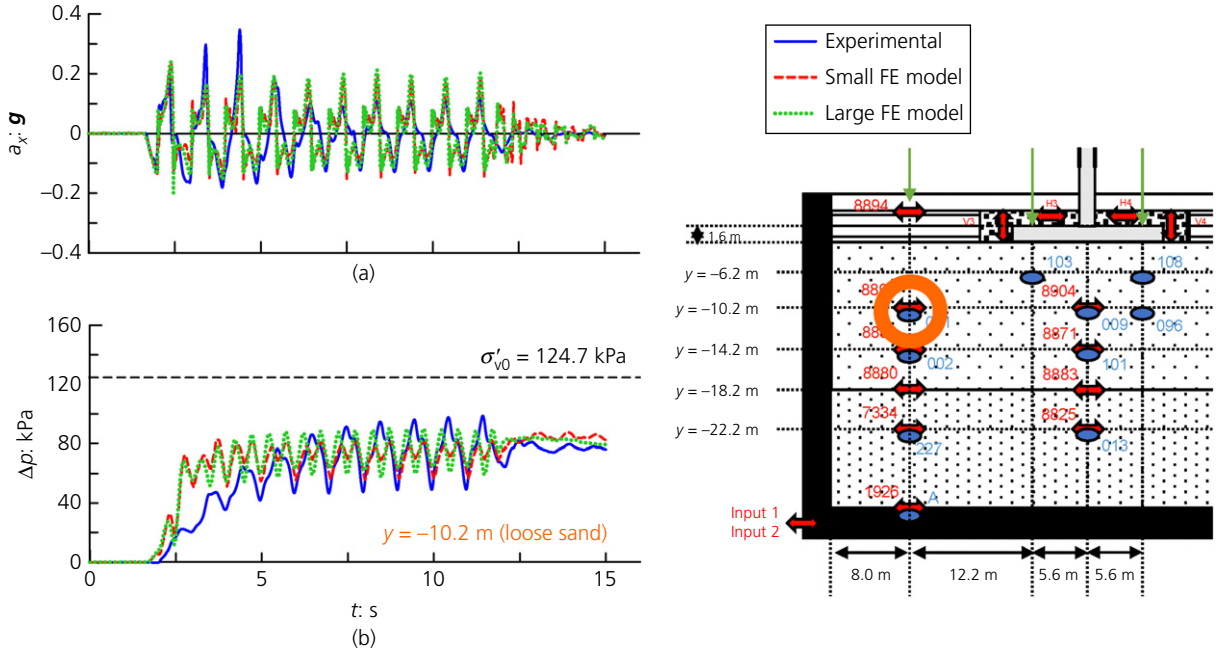

Figure 14. (a) Total horizontal acceleration and (b) excess pore-water pressure time histories computed along the far-field alignment with the small and large FE models, together with those recorded in the centrifuge

and large FE models, namely the scaled Imperial Valley (I) and Kobe (K) acceleration time histories, characterised by peak accelerations $a_{x\,\max}^{\text{inp}} \approx 0.07\boldsymbol{g}$, and $a_{x\,\max}^{\text{inp}} \approx 0.03\boldsymbol{g}$, respectively (Figure 17). These seismic inputs had been applied in the centrifuge tests and had not triggered liquefaction in the loose sand layer, due to their low intensity. As already discussed for the sinusoidal motion, the comparison of results obtained with the small and large FE models shows that the boundary effects caused an increase of both the peak relative settlement and rotation of the raft foundation (Figure 18(a)). Therefore, the predictions obtained with the small model (and the results of the centrifuge tests) are on the safe side, but the difference with the proper large model are quite low, and they reduce with decreasing amplitude of the seismic input. A clear trend cannot be established for the seismic performance of the tower (Figure 18(b)). However, the difference between the results of

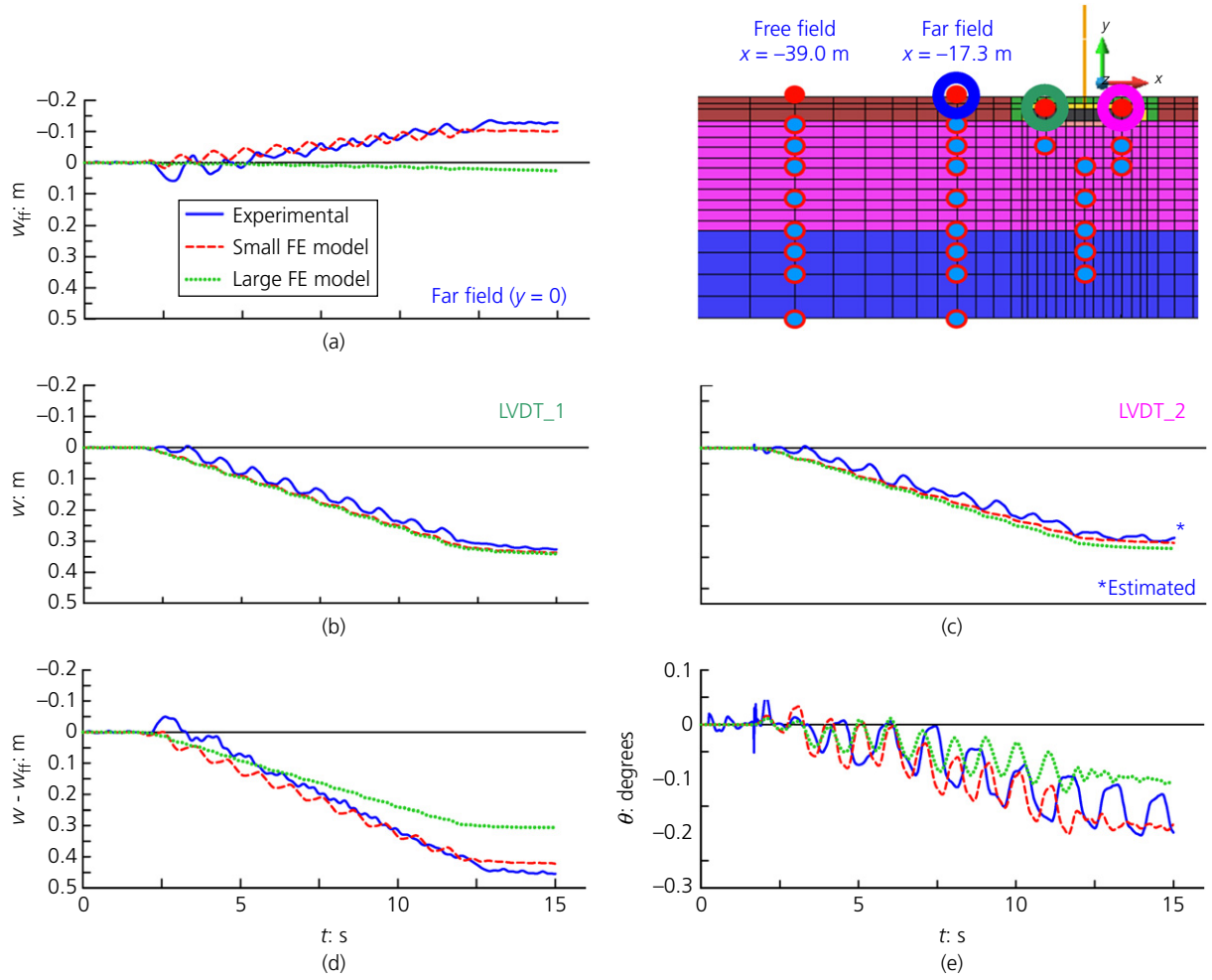

Figure 15. Time histories of (a) settlements at the far-field ground surface and (b–c) at both foundation sides, (d) of the average settlement relative to the far field and (e) of rotation time histories obtained with the small and large FE models, together with those recorded in the centrifuge

the small and big FE model is of the order of 18%, as confirmed by the ratios large/small listed in Table 5.

6. Concluding remarks

In this paper, the influence of flexible boundaries of the ESB container has been assessed, to gain more awareness of results coming from centrifuge testing, which has been established as a powerful tool in the field of physical modelling in geotechnics.

To this end, a case example of an onshore wind turbine resting on liquefiable soils and subjected to a strong sine wave, capable of triggering liquefaction into the loose sand layer, has been first tested in the Turner beam centrifuge available at Schofield Centre, University of Cambridge. Experimental results have been therefore reproduced by a 3D numerical FE model implemented in the OpenSees framework, reproducing the ESB box size and boundary conditions. Mechanical behaviour of foundation soils has been simulated through the advanced Sanisand04 constitutive model, while the bi-phase nature of soils has been reproduced through the *u–p* formulation: hydro-mechanical soil parameters have been calibrated against the far-field results obtained in the centrifuge, and this turned out to provide a surprisingly good 'blind' prediction of the seismic performance of the structure at hand. Boundary effects on the OWT seismic performance have then been evaluated by comparing the numerical results computed with the numerical model reproducing the ESB box (small model) with those obtained with a much larger and rigorous domain (large model), where wall ends affect neither the results at the far-field array nor the structure behaviour.

The comparison showed that the array usually taken as far field in the ESB container is not significantly affected by the

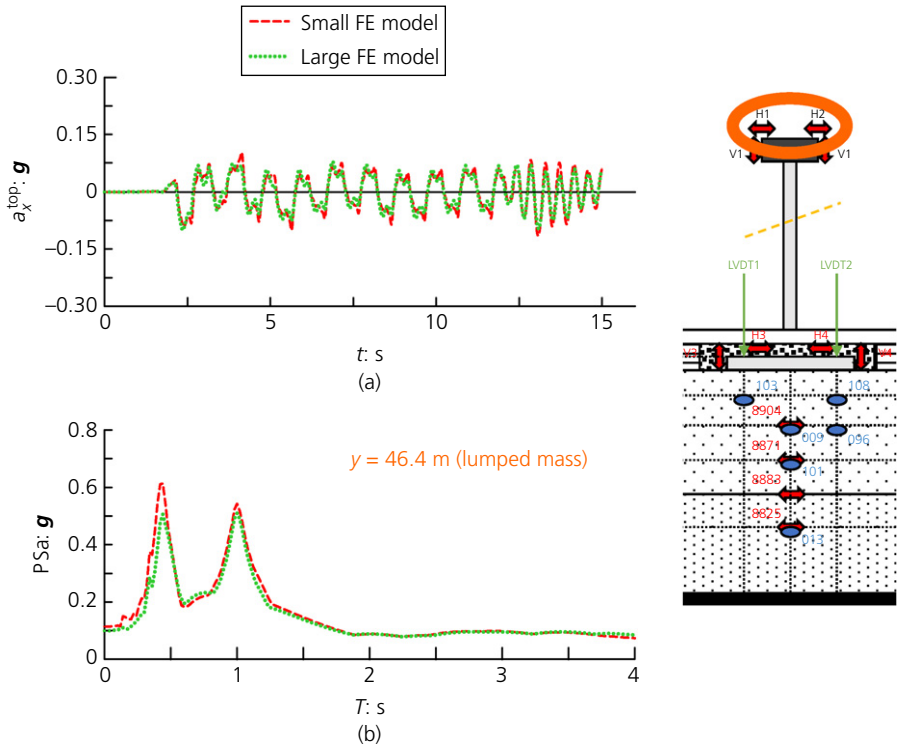

Figure 16. (a) Total horizontal acceleration time histories and (b) elastic acceleration spectra obtained at the lumped mass level with the small and large FE model

Table 5. Comparison of seismic performance indexes from the small and large models

Input	Sinusoidal (S)			Scaled Imperial Valley (I)			Scaled Kobe (K)		
Index	Small	Large	Large/small	Small	Large	Large/small	Small	Large	Large/small
$(w–w_{ff})_{max}$: m	0.42	0.31	0.73	0.13	0.08	0.60	0.01	0.00	0.37
θ_{max}: °	0.20	0.12	0.62	0.05	0.04	0.94	0.01	0.00	0.51
a_{xmax}^{top}: ***g***	0.11	0.10	0.87	0.16	0.17	1.07	0.03	0.04	1.12
PSa (T = 0.44 s): ***g***	0.61	0.51	0.83	0.54	0.67	1.25	0.17	0.22	1.32

presence of the vertical boundaries when looking at horizontal accelerations and excess pore-water pressures, whereas settlement at ground surface shows non-negligible deviation caused by the proximity of wall ends. Nevertheless, displacements of the raft foundation and inertial forces transmitted to the superstructure are very slightly influenced by the presence of the end walls, except for some high-frequency components which can be attributed to P-waves generated at the soil–boundary contacts. Boundary effects were quantified in terms of the difference between the values attained by some selected seismic performance indexes evaluated with the small and large numerical models, namely: the peak values of the relative settlement between the raft foundation and the far-field ground surface, of the rigid rotation of the foundation, and of the horizontal acceleration transmitted to the top of the OWT. Without considering the very-low intensity seismic input, for which permanent displacement and tilting of the raft foundation were almost zero, a maximum difference of about 40% was obtained for the settlement of the raft foundation for a low-intensity seismic shaking, for which liquefaction in the saturated sandy soil did not occur. Conversely, for the high-intensity seismic input, which triggered liquefaction in the sandy soil, a maximum difference of about 38% was computed for the raft rotation. This corresponds to a modest deviation, of 0.08°, which can be considered negligible if compared with the permanent tilt of about 0.50–0.75° typically allowed for wind turbines. As for the remaining seismic indexes adopted in this study, the average difference is less than 20%, which

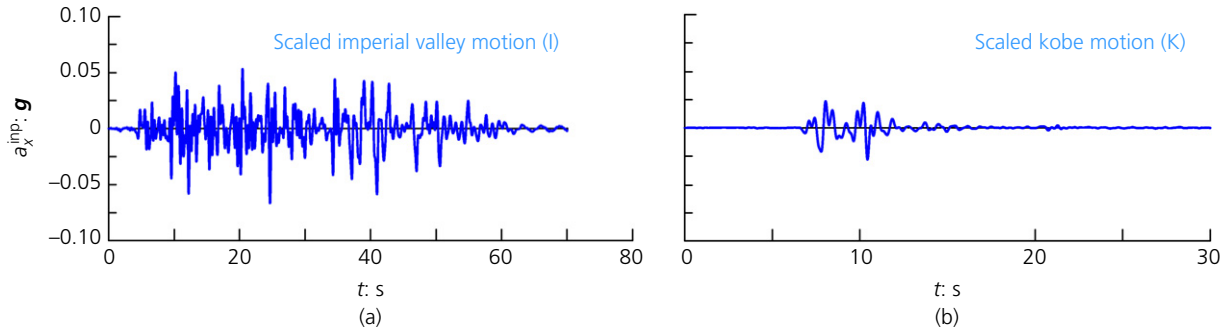

Figure 17. Additional inputs considered in the study: scaled (a) Imperial Valley and (b) Kobe motions

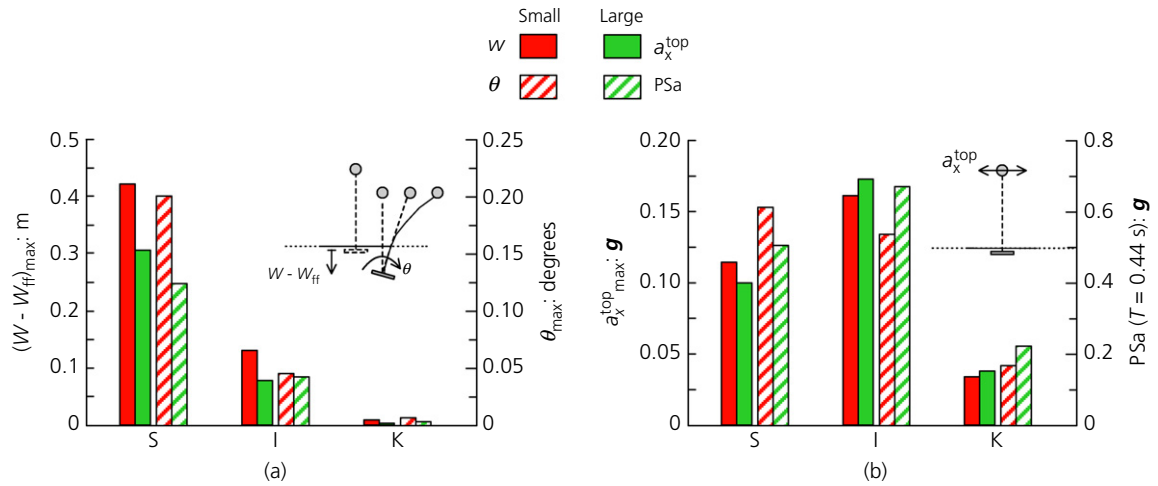

Figure 18. Seismic performance indexes computed for (a) the raft foundation and (b) the wind turbine with the small and large FE model for the three inputs considered in the study: sinusoidal (S), scaled Imperial Valley (I) and Kobe (K) motions

confirms the reliability of dynamic centrifuge testing when assessing the seismic performance of structures even on liquefiable soils. However, boundaries affected also the vertical displacements experienced by ground surface in the far field, where a noticeable heave was recorded in the centrifuge and obtained from the small FE model, while a slight settlement was calculated using the large FE model.

The novelty of this paper lies in the evaluation of boundary effects in the presence of soft and saturated sandy soils subjected to both strong and weak seismic events, the former capable of making the stiffness ratio between end wall and foundation soils strongly increase due to liquefaction. The results obtained in this study may be taken as a reference when interpreting results coming from dynamic centrifuge tests, as they provide a quantitative measurement of boundary effects on the seismic performance of slender structures on liquefiable soils. Moreover, calibration of Hostun sand parameters for the Sanisand04 model against dynamic centrifuge tests constitutes a novel and useful outcome as well, as Hostun HN31 sand is widely used for research purposes.

Acknowledgements

The centrifuge experiment was performed with the help of technicians at the Schofield Centre of Cambridge University. This support is acknowledged.

REFERENCES

Adamidis O and Madabhushi SPG (2015) Use of viscous pore fluids in dynamic centrifuge modelling. *International Journal of Physical Modelling in Geotechnics* **15(3)**: 141–149, https://doi.org/10.1680/jphmg.14.00022.

Adamidis O and Madabhushi SPG (2022) Rocking response of structures with shallow foundations on thin liquefiable layers. *Géotechnique* **72(2)**: 127–145, https://doi.org/10.1680/jgeot.19.P.077.

Azeiteiro RJN, Coelho PALF, Taborda DMG and Grazina JCD (2017) Critical state-base interpretation of the monotonic behaviour of Hostun sand. *Journal of Geotechnical and Geoenvironmental Engineering* **143(5)**: 04017004.

Boulanger RW and Ziotopoulou K (2013) Formulation of a sand plasticity plane-strain model for engineering applications. *Soil Dynamics and Earthquake Engineering* **53**: 254–267.

Brennan AJ and Madabhushi SPG (2002) Design and performance of a new deep model container for dynamic centrifuge testing. In *Physical Modelling in Geotechnics – ICPMG '02* (Phillips R, Guo PJ and Popescu R (eds)). Balkema, Rotterdam, The Netherlands, pp. 183–188.

Chen L, Ghofrani A and Arduino P (2021) Remarks on numerical simulation of the LEAP-Asia-2019 centrifuge tests. *Soil Dynamics and Earthquake Engineering* **142**: 106541.

Dafalias YF and Manzari MT (2004) Simple plasticity sand model accounting for fabric change effects. *Journal of Engineering Mechanics* **130(6)**: 622–634.

Dashti S, Bray JD, Pestana JM, Riemer M and Wilson D (2010) Mechanisms of seismically induced settlement of buildings with shallow foundations on liquefiable soil. *Journal of Geotechnical and Geoenvironmental Engineering* **144(10)**: 04018073.

Esfeh PK and Kaynia AM (2020) Earthquake response of monopiles and caissons for offshore wind turbines. *Soil Dynamics and Earthquake Engineering* **136**: 106213.

Ghosh B and Madabhushi SPG (2002) An efficient tool for measuring shear wave velocity in the centrifuge. In *Physical Modelling in Geotechnics – ICPMG '02* (Phillips R, Guo PJ and Popescu R (eds)). Balkema, Rottedam, the Netherlands, pp. 119–124.

Griffiths DV (1985) Numerical modelling of interfaces using conventional finite elements. In *Numerical Methods in Geomechanics Nagoya 1985* (Kawamoto T and Ichikawa Y (eds)). Balkema, Rotterdam, the Netherlands, pp. 837–844.

Haigh SK, Ghosh B and Madabhushi SPG (2005) The effect of time step discretisation on dynamic finite element analysis. *Canadian Geotechnical Journal* **42(3)**: 957–963, https://doi.org/10.1139/T05-022.

Haigh SK, Eadington J and Madabhushi SPG (2012) Permeability and stiffness of sands at very low effective stresses. *Géotechnique* **62(1)**: 69–75, https://doi.org/10.1680/geot.10.P.035.

Karimi Z (2016) *Seismic Performance of Shallow-Founded Structures on Liquefiable Ground: an Experimental and Numerical Study.* PhD dissertation, University of Colorado Boulder, Boulder, CO, USA.

Kassas K, Adamidis O, Gerolymos N and Anastasopoulos I (2021) Numerical modelling of a structure with shallow strip foundation during earthquake-induced liquefaction. *Géotechnique* **71(12)**: 1099–1113, https://doi.org/10.1680/jgeot.19.P.277.

Kaynia AM (2019) Seismic considerations in design of offshore wind turbines. *Soil Dynamics and Earthquake Engineering* **124**: 399–407.

Kementzetzidis E, Corciulo S, Versteijen WG and Pisanò F (2019) Geotechnical aspects of offshore wind turbine dynamics from 3D non-linear soil-structure simulations. *Soil Dynamics and Earthquake Engineering* **120**: 181–199.

Kuhlemeyer RL and Lysmer J (1973) Finite element method accuracy for wave propagation problems. *Journal of the Soil Mechanics and Foundation Division* **99(5)**: 421–426.

Liu HY, Kementzetzidis E, Abell JA and Pisanó F (2021) From cyclic sand ratcheting to tilt accumulation of offshore monopiles: 3D FE modelling using SANISAND-MS. *Géotechnique*, https://doi.org/10.1680/jgeot.20.P.029.

Madabhushi SPG, Houghton NE and Haigh SK (2006) A new automatic sand pourer for model preparation at University of Cambridge. In *Physical Modelling in Geotechnics – ICPMG '06* (Ng CWW, Zhang LM and Wang YH (eds)). Taylor & Francis Group, London, UK, pp. 217–222.

Manzari MT, El Ghoraiby M, Kutter BL *et al.* (2018) Mechanisms of seismically induced settlement of buildings with shallow foundations on liquefiable soil. *Soil Dynamics and Earthquake Engineering* **113**: 714–743.

McKenna F, Fenves GL, Scott MH and Jeremić B (2000) *Open System for Earthquake Engineering Simulation*. University of California Berkeley, Berkeley, CA, USA. See http://opensees.berkeley.edu (accessed 19/04/2022).

Newmark NM (1959) A method of computation for structural dynamics. *Journal of Engineering Mechanics Division* **85(EM3)**: 67–94.

Pisanò F (2019) Input of advanced geotechnical modelling to the design of offshore wind turbine foundations. In *Proceedings of the XVII ECSMGE-2019: Geotechnical Engineering – Foundation of the Future* (Sigursteinsson H, Erlingsson S and Bessason B (eds)). Icelandic Geotechnical Society (IGS), Reykjavík, Iceland, pp. 272–297.

Ramirez J (2019) *Performance of Inelastic Structures on Mitigated and Unmitigated Liquefiable Soils: Evaluation of Numerical Simulations with Centrifuge Tests.* PhD dissertation, University of Colorado Boulder, Boulder, CO, USA.

Ramirez J, Barrero AR, Chen L *et al.* (2018) Site response in a layered liquefiable deposit: evaluation of different numerical tools and methodologies with centrifuge experimental results. *Journal of Geotechnical and Geoenvironmental Engineering* **136(1)**: 151–164.

Salvatore E, Proia R, Modoni G, Andò E and Viggiani G (2017) Influenza delle condizioni sperimentali delle prove triassiali su sabbie. *Incontro Annuale dei Ricercatori di Geotecnica 2017 – IARG 2017, Matera, Italy* (in Italian).

Schofield AN and Zeng X (1992) *Design and Performance of an Equivalent Shear Beam (ESB) Container for Earthquake Centrifuge Modelling*. Department of Engineering, University of Cambridge, Cambridge, UK, Technical report TR245.

Scott MH and Fenves GL (2010) Krylov subspace accelerated Newton algorithm: application to dynamic progressive collapse simulation of frames. *Journal of Structural Engineering* **136(5)**: 473–480.

Tarque Ruiz SN (2020) *Programa Compilado OpenSees, Mayo 2020*. Pontificia Universidad Católica del Perú, Lima, Peru. See https://drive.google.com/file/d/1ETGQ3Y9HOmxdfyA6k2edwwYo0zW5Mk7C/view?usp=sharing (accessed 19/04/2022).

Teymur B and Madabhushi SPG (2003) Experimental study of boundary effects in dynamic centrifuge modelling. *Géotechnique* **53(7)**: 655–663, https://doi.org/10.1680/geot.2003.53.7.655.

Tsinidis G, Pitilakis J, Madabhushi SPG and Heron C (2015) Dynamic response of flexible square tunnels: centrifuge testing and validation of existing design methodologies. *Géotechnique* **65(5)**: 401–417, https://doi.org/10.1680/geot.SIP.15.P.004.

Yang Z, Elgamal A and Parra E (2003) A computational model for liquefaction and associated shear deformation. *Journal of Geotechnical and Geoenvironmental Engineering* **129(12)**: 1119–1127.

Yang Z, Lu J and Elgamal A (2008) *OpenSees Soil Models and Solid-Fluid Fully Coupled Elements: User's Manual*. Department of Structural Engineering, University of California, San Diego, CA, USA.

Yang M, Taiebat M and Dafalias YF (2022) SANISAND-MSf: a sand plasticity model with memory surface and semifluidised state. *Géotechnique* **72(3)**: 227–246. https://doi.org/10.1680/jgeot.19.P.363.

Zienkiewicz OC and Shiomi T (1984) Dynamic behaviour of saturated porous media; the generalized Biot formulation and its numerical solution. *International Journal for Numerical and Analytical Methods in Geomechanics* **8(1)**: 71–96.

Zienkiewicz OC, Chang CT and Bettes P (1980) Drained, undrained, consolidating and dynamic behaviour assumptions in soils. *Géotechnique* **30(4)**: 385–395, https://doi.org/10.1680/geot.1980.30.4.385.

Zienkiewicz OC, Bianic N and Shen FQ (1988) Earthquake input definition and the transmitting boundary condition. In *Advances in Computational Non-linear Mechanics* (Doltsinis IS (ed.)). Springer, Vienna, Austria, vol. 300, pp. 109–138.